Supplementary information of
"Critical influence of aggregate types on the compressive strength of concrete"

Ippei Maruyama[1,2,*], Sou Sugimoto[3]

1: Professor, Department of Architecture, The University of Tokyo
2: Professor, Department of Environmental Engineering and Architecture, Nagoya University
3: Graduate student, Department of Environmental Engineering and Architecture, Nagoya University
*: corresponding author

1. Constitutive laws of mortar, aggregate, and interfacial zone for Rigid Body Spring Network Model (RBSM)

Spring parameters

(a) Stress and strain

σ^*, σ^{T*}: Stress and stress at the maximum strain in history of the normal springs, respectively (N/mm^2)

ε^*, ε^{T*}: Strain and maximum strain in history of the normal springs, respectively (-)

ε_t^*: Strain at the tensile strength (f_{tm}^*, f_{ta}^*, $f_{t,ITZ}^*$) in the normal springs (-)

w_{cr}^*: Crack width of the normal springs (mm)

h^*: Length of spring (mm)

τ^*, τ^{T*}: Shear stress and stress at the maximum shear strain in the history of the shear springs, respectively (N/mm^2)

γ^*, γ^{T*}, γ^{pl*}: Shear strain, maximum shear strain in the history, and plastic shear strain of the shear springs, respectively (-)

τ_f^*, γ_f^*: Shear strength (N/mm^2) and strain at the shear strength (-) of the shear springs, respectively

(b) Mortar and aggregate

f^*_{tm}, f^*_{ta}: Tensile strength of normal springs for mortar and aggregate, respectively (N/mm^2)

G_{ftm}^*, G_{fta}^*: Fracture energy of normal springs for mortar and aggregate, respectively (N/mm)

c_m^*, c_a^*: Cohesion of shear springs of mortar and aggregate, respectively (N/mm^2)

E_{cm}^*, E_{ca}^*: Young's moduli of normal springs of mortar and aggregate, respectively (N/mm^2)

G_m^*, G_a^*: Shear moduli of shear springs for mortar and aggregate, respectively (N/mm^2)

η^*: Ratio of the shear modulus and Young's modulus of springs (G^*/E_c^*) (-)

Spring parameters (continued)

σ_b^*: Constant to determine the limit of the shear strength increase (N/mm^2)

φ^*: Internal friction angle of the shear spring (degrees)

K^*: Softening slope of the shear spring (N/mm^2)

β_0^*, χ^*, β_{max}^*: Constants for the shear softening slope (K^*) (-)

β_{cr}^*: Shear reduction factor (with increasing crack width, shear stress is reduced) (-)

κ^*: Constant for β_{cr}^* (-)

(c) ITZ

$f_{t,ITZ}^*$: Tensile strength of the ITZ spring (for the RBSM spring parameter) ($f_{t,ITZ}^* = \beta_{\mathrm{ITZ}} f_{tm}^*$) (N/mm^2)

$G_{ft,ITZ}^*$: Fracture energy of the ITZ spring ($G_{ft,ITZ}^* = \eta_{\mathrm{ITZ}}\, G_{ftm}^*$) (N/mm^2)

c_{ITZ}^*: Cohesion of the ITZ spring ($c_{ITZ}^* = \beta_{\mathrm{ITZ}}\, c_m^*$) (N/mm^2)

$E_{c,ITZ}^*$, $E_{t,ITZ}^*$: Young's modulus of the ITZ spring in compression ($E_{c,ITZ}^* = \gamma_{\mathrm{ITZ}}\, E_{cm}^*$) and in tension ($E_{t,ITZ}^* = \alpha_{\mathrm{ITZ}}\, E_{cm}^*$), respectively (N/mm^2)

G_{ITZ}^*: Shear modulus of the ITZ ($G_{ITZ}^* = \alpha_{\mathrm{ITZ}}\, G_m^*$) (N/mm^2)

d_{ITZ}: thickness of the ITZ layer (mm)

This section is based on previous research [22,23]. The RBSM models a continuous material as an assembly of rigid particle elements interconnected by springs along their boundaries (Supplementary Figure 1). The strain of the springs was calculated by dividing the relative displacement between two adjacent elements by the initial distance between those elements (h^* (= h_i^*+h_j^*) in Supplementary Figure 1(b)).

In the model, each interface between two rigid particles was divided into several triangles formed by the barycenter and two adjacent vertices of the surface, with each triangle having three individual springs: one for the normal force and two for the orthogonal tangential forces (Supplementary Figure 1(a)). Voronoi tessellation was applied[51] for the random directional progression of cracks.

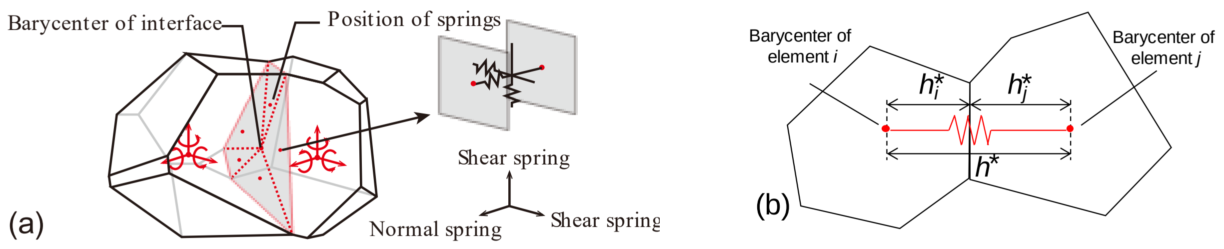

Supplementary Figure 1. Schematic of RBSM, showing a) the relationship between elements and springs, with the same number of springs on an interface as the number of face vertices, and b) the definition of spring length h^*

The constitutive laws originally developed for concrete[52,53] were introduced to the mortar and aggregate springs, as shown in Fig. ?. The compressive behavior was completely elastic. The tensile behavior of the mortar and aggregate was linearly elastic until the stress reached the tensile strength, after which the mortar and aggregate softened according to a 1/4-model (Supplementary Figure 2(a))[54]. The skeleton curve in tension is given by

$$\sigma^* = \begin{cases} E_c^*\varepsilon^* & (\varepsilon^* < \varepsilon_t^*) \\ f_t^* + \dfrac{0.25f_t^* - f_t^*}{\varepsilon_{tl}^* - \varepsilon_t^*}(\varepsilon^* - \varepsilon_t^*) & (\varepsilon_t^* < \varepsilon^* < \varepsilon_{tl}^*) \\ 0.25f_t^* + \dfrac{-0.25f_t^*}{\varepsilon_{tu}^* - \varepsilon_{tl}^*}(\varepsilon^* - \varepsilon_{tl}^*) & (\varepsilon_{tl}^* < \varepsilon^* < \varepsilon_{tu}^*) \\ 0 & (\varepsilon_{tu}^* < \varepsilon^*) \end{cases}, \qquad \text{(s1)}$$

where the tensile strength f^*_{tm} (or f^*_{ta}), fracture energy G_{ftm}^* (or G_{fta}^*), Young's modulus E_{cm}^* (or E_{ca}^*), and spring length h^* are constants for the tension field; $\varepsilon_t^* = f_t^*/E_c^*$, $\varepsilon_{tl}^* = 0.75G_{ft}^*/(f_t^* \cdot h^*) + \varepsilon_t^*$, and $\varepsilon_{tu}^* = 5.0G_{ft}^*/(f_t^* \cdot h^*) + \varepsilon_t^*$.

The shear stress–strain skeleton curve of the tangential springs (Supplementary Figure 2(b)) is given by

$$\tau^* = \begin{cases} \beta_{cr}^* G^* \gamma^* & (\gamma^* \le \gamma_f^*) \\ \beta_{cr}^* max(\tau_f^* + K^*(\gamma^* - \gamma_f^*), 0.1\tau_f^*) & (\gamma^* > \gamma_f^*) \end{cases}, \qquad \text{(s2)}$$

where γ^* is the shear strain; G^* is the shear stiffness (G_m^* or G_a^*) (N/mm^2); τ_f^* is the shear strength (Eq. (s4)) (N/mm^2); K^* is the softening slope; β_{cr}^* is the shear reduction coefficient (Eq. (s5)), and γ_f^* is the strain at $\beta_{cr}^*\tau_f^*$ (=τ_f^*/G^*). The shear stress increases linearly with shear stiffness G^* until the shear strength τ_f^* is reached. The softening slope K^* varies with the stress of the normal spring (σ^*), as shown in Supplementary Figure 2(c), and is given by

$$K^* = \min(\beta_0^* + \chi^*(\sigma^*/\sigma_b^*), \beta_{max}^*) \cdot G^*, \qquad \text{(s3)}$$

where β_0^*, χ^*, and β_{max}^* are constants defining K^*. Following the Mohr–Coulomb criteria as shown in Supplementary Figure 2(d), τ_f^* is given by

$$\tau_f^* = \begin{cases} c^* - \sigma^* \tan\varphi^* & (\sigma^* > -\sigma_b^*) \\ c^* + \sigma_b^* \tan\varphi^* & (\sigma^* < -\sigma_b^*) \end{cases}, \qquad \text{(s4)}$$

where c^* is the cohesion (c_m^* or c_a^*) (N/mm^2); φ^* is the angle of internal friction (degrees); σ^* is the stress of the normal spring (N/mm^2), and σ_b^* is a constant used to determine the limit of the increase in shear strength. The decrease in shear transfer due to the crack in the normal spring is denoted as β_{cr}^*, as shown in Supplementary Figure 2(e), and is given by

$$\beta_{cr}^* = \min\left(\frac{\varepsilon_t^*}{\varepsilon^*}\exp\left\{\frac{\kappa^*}{\varepsilon_{tu}^*}(\varepsilon^* - \varepsilon_t^*)\right\}, 1.0\right), \qquad \text{(s5)}$$

where ε^* is the strain of the normal spring; ε_t^* is the cracking strain; ε_{tu}^* is the strain after complete softening (Supplementary Figure 2(a)), and κ^* is a constant. Before cracks occur in the corresponding normal spring, β_{cr}^* is 1.0.

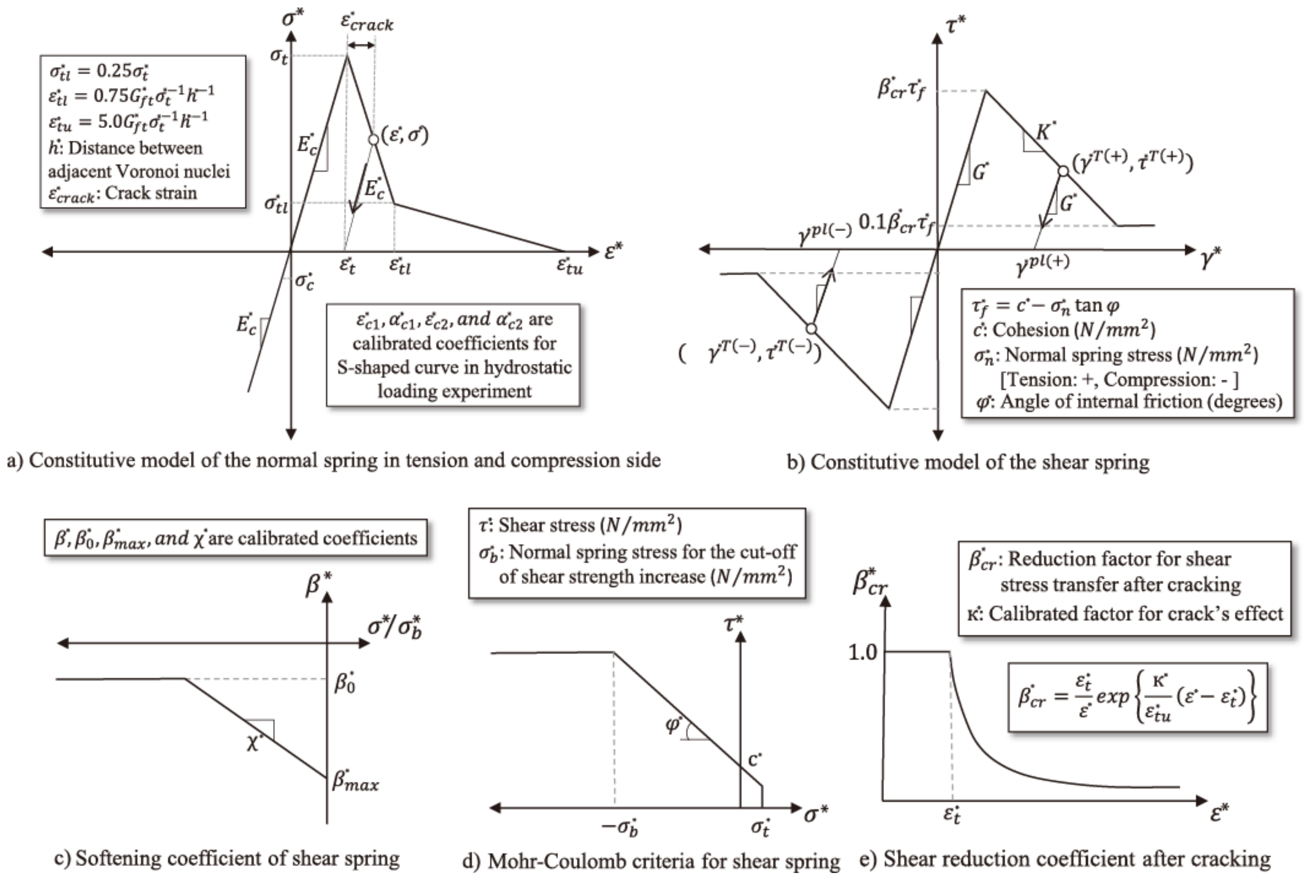

Supplementary Figure 2. Constitutive laws of the mortar and aggregate: (a) tensile model of normal spring; (b) shear spring model; (c) softening coefficient of shear spring; (d) Mohr–Coulomb criteria for shear spring; (e) shear reduction coefficient. E_c^* is E_{cm}^* for mortar and E_{ca}^* for aggregate. Similarly for f_t^*, G_{ft}^*, G^*, and c^*, the subscripts *m* and *a* denote mortar and aggregate, respectively. (after 52)

Supplementary Figure 3 shows the cyclic behaviors of the normal and shear springs. In the normal spring, the unloading stiffness is the same as E_c^*; the reloading stiffnesses $E_{c,re}^*$ are expressed as

$$E_{re}^* = \frac{(\sigma^{T*} - \sigma^*)}{(\varepsilon^{T*} - \varepsilon^*)}, \qquad \text{(s6)}$$

where σ^* and ε^* are the current stress and strain ($\varepsilon^* > 0$), respectively. Under shear, the unloading and reloading stiffness are the same as the shear modulus (G^* in Eq. (s2)). The reloading shear stress τ_{re}^* (see Paths 5 and 6 in Supplementary Figure 3(b)) is given by

$$\tau_{re}^* = \begin{cases} -\beta_{cr}^* max\left(\tau_f^* + K^*\left(|\gamma^*| - \gamma_f^*\right), 0.1\tau_f^*\right) & \left(|\gamma^{T*}| < |\gamma^*|, 0 > \gamma^*\right) \\ \beta_{cr}^* max\left\{\left(\gamma^* - \gamma^{pl(-)*}\right)G^*, -|\tau^{T*}|\right\} & \left(-|\gamma^{T*}| < \gamma^* < \gamma^{pl(-)*}\right) \\ 0 & \left(\gamma^{pl(-)*} < \gamma^* < \gamma^{pl(+)*}\right) \\ \beta_{cr}^* min\left\{\left(\gamma^* - \gamma^{pl(+)*}\right)G^*, |\tau^{T*}|\right\} & \left(\gamma^{pl(+)*} < \gamma^* < \gamma^{T*}\right) \\ \beta_{cr}^* max\left(\tau_f^* + K^*\left(\gamma^* - \gamma_f^*\right), 0.1\tau_f^*\right) & \left(|\gamma^{T*}| < |\gamma^*|, 0 < \gamma^*\right) \end{cases}, \text{ where} \qquad \text{(s7)}$$

$$\gamma^{T*} = max\left(|\gamma^{T(-)*}|, \gamma^{T(+)*}\right), \qquad \text{(s8)}$$

and

$$\gamma^{pl(+)*} = \gamma^{T(+)*} - \tau^{T(+)*}/G^* \text{ and} \qquad \text{(s9)}$$

$$\gamma^{pl(-)*} = \gamma^{T(-)*} - \tau^{T(-)*}/G^*, \qquad \text{(s10)}$$

where γ^{T*} is the absolute total shear strain (the historical maximum strain in absolute value); $\gamma^{T(+)*}$ and $\gamma^{T(-)*}$ are the total shear strains in positive and negative directions, respectively; $\gamma^{pl(+)*}$ and $\gamma^{pl(-)*}$ are the positive and negative plastic strains, respectively; $\tau^{T(+)*}$ and $\tau^{T(-)*}$ are the stresses on the skeleton curve at $\gamma^{T(+)*}$ and $\gamma^{T(-)*}$ (Supplementary Figure 2(b)), respectively. $\pm\beta_{cr}^* max\left(\tau_f^* + K^*\left(|\gamma^*| - \gamma_f^*\right), 0.1\tau_f^*\right)$ in Eq. (s7) indicates the skeleton curve in the shear (Eq. (s2)).

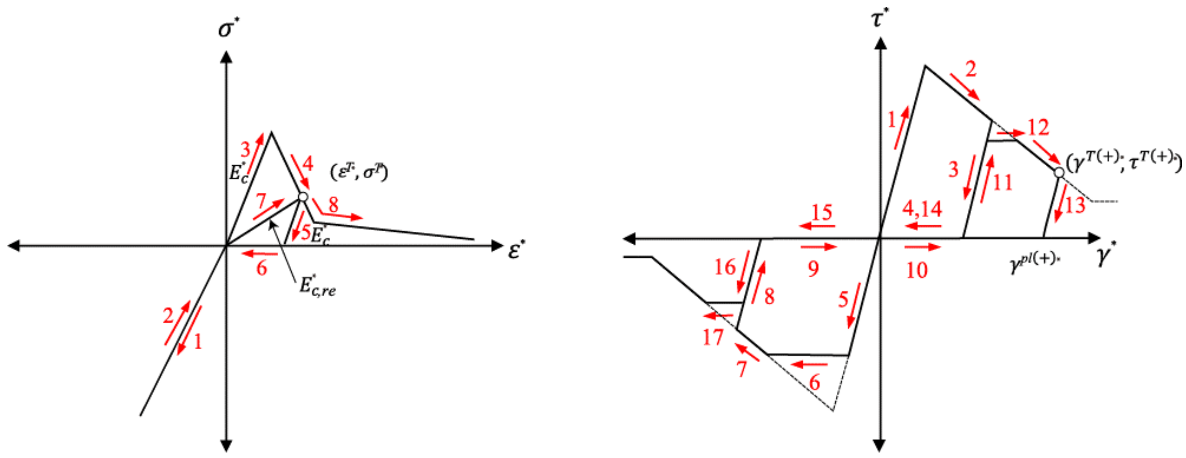

a) Normal spring b) Shear spring

Supplementary Figure 3. Hysteresis of stress–strain relationship for (a) the normal spring; (b) the shear spring under a constant normal stress of σ^* (after 53)

Supplementary Figure 4 shows the constitutive model of the ITZ and the interface between the mortar and coarse aggregate for the normal spring. A 1/4-scale softening model (similar to a mortar model) was used for the tension field. For the compressive field, the initial Young's modulus ($E_{c,ITZ}^*$) was reduced until the strain was larger than $-\varepsilon_{ITZ}^*$, and the Young's modulus was set to the average of the two material stiffnesses weighted by h_i^* and h_j^*, as shown in Supplementary Figure 2(b). ε_{ITZ}^* is given by

$$\varepsilon_{ITZ}^* = d_{ITZ}/h^*, \qquad \text{(s11)}$$

where d_{ITZ} denotes the effective thickness of the ITZ layer (mm). This ITZ behavior assumes that the ITZ is compacted in compression, and the coarse aggregate and mortar come into contact with a higher stiffness[23]. After the compressive strain exceeded $-\varepsilon^*_{ITZ}$, the linear elastic model was implemented.

In the shear field, the cohesion of the ITZ spring (c^*_{ITZ}) was set as a constant scalar multiple of the mortar properties, as shown in Supplementary Figure 4(b). The other shear parameters (Supplementary Figure 2(c)–(e)) were the same as those for the mortar. The internal friction angle φ^* of the ITZ was also set to the same as that of the mortar (37°), similar to previous experimental studies (approximately 35°) [59,60].

Some ITZ properties (f^*_t, G^*_{ft}, E^*_c, G^*, and c^*, as shown in Supplementary Figure 2(a)–(c)) were set as constant multiple coefficients (α_{ITZ}, β_{ITZ}, γ_{ITZ}, and η_{ITZ}, as shown in Supplementary Figure 4) of the mortar properties. The coefficients were determined by fitting the experimental results (3.2 of 23). Next, we discuss the effects of these parameters on the results. The same unloading and reloading laws as those used for the mortar spring (Supplementary Figure 3) were applied to the ITZ normal and shear springs. The stress–strain curve of the ITZ in compression is always on the skeleton curve shown in Supplementary Figure 4(a).

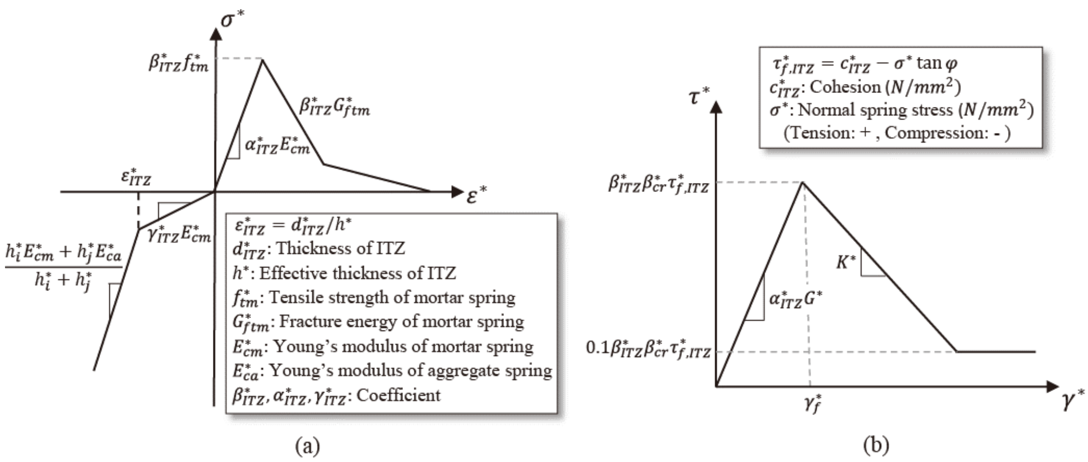

Supplementary Figure 4. Constitutive law of mortar–aggregate interface (ITZ): (a) tension and compression; (b) shear

2. Spring parameter input using macroscopic material properties

Unlike the finite element method, the RBSM does not directly use the macroscopic material properties as parameters for spring constitutive models. Thus, the spring parameters were evaluated to reproduce several types of material tests; these calibration processes were necessary to reproduce realistic behavior [23,52,16]. Based on the calibrations presented in reference [23], the parameters presented in Supplementary Table 1 were used. $f_{cm,macro}$, $f_{ca,macro}$ represent the macroscopic experimental compressive strengths of the mortar and aggregate, respectively (N/mm^2); $f_{tm,macro}$, $f_{ta,macro}$ represent the macroscopic experimental splitting tensile strengths of the mortar and aggregate, respectively (N/mm^2); $E_{cm,macro}$, $E_{ca,macro}$ represent the macroscopic experimental Young's moduli of the mortar and aggregate, respectively (N/mm^2); $G_{ftm,macro}$, $G_{fta,macro}$ represent the macroscopic experimental fracture energies of the mortar and aggregate, respectively (N/mm^2).

Supplementary Table 1. Relationships between spring parameters and macroscopic material properties

(a) Normal spring

	Young's modulus	Tension field	
	E_c^*	f_t^*	G_{ft}^*
Mortar	$1.45E_{cm,macro}$	$1.0f_{tm,macro}$	$0.5G_{ftm,macro}$
Aggregate	$1.45E_{ca,macro}$	$1.0f_{ta,macro}$	$0.5G_{fta,macro}$

(b) Shear spring

<table>
<tr><th></th><th>Shear modulus</th><th colspan="3">Failure criteria</th><th colspan="4">Softening behavior</th></tr>
<tr><th></th><th>$\eta^*=G^*/E_c^*$</th><th>c^*</th><th>φ^*</th><th>σ_b^*</th><th>β_0^*</th><th>β_{max}^*</th><th>χ^*</th><th>κ^*</th></tr>
<tr><td>Mortar</td><td rowspan="7">0.35</td><td>$0.14f_{cm,macro}$</td><td rowspan="7">37</td><td>$0.55f_{cm,macro}$</td><td rowspan="2">−0.05</td><td rowspan="7">−0.025</td><td rowspan="7">−0.01</td><td rowspan="7">−0.3</td></tr>
<tr><td>Aggregate (elastic)</td><td>$0.14f_{ca,macro}$</td><td rowspan="6">$0.55f_{ca,macro}$</td></tr>
<tr><td>($f_{ca,macro}$ =40 MPa)</td><td>$0.15f_{ca,macro}$</td><td rowspan="5">−0.10</td></tr>
<tr><td>($f_{ca,macro}$ =50 MPa)</td><td>$0.16f_{ca,macro}$</td></tr>
<tr><td>($f_{ca,macro}$ =100 MPa)</td><td>$0.19f_{ca,macro}$</td></tr>
<tr><td>($f_{ca,macro}$ =150 MPa)</td><td>$0.22f_{ca,macro}$</td></tr>
<tr><td>($f_{ca,macro}$ =200 MPa)</td><td>$0.25f_{ca,macro}$</td></tr>
</table>

The superscript * indicates the spring parameters; the subscript 'macro' indicates macroscopic material properties.

(c) ITZ parameters

α_{ITZ}	η_{ITZ}	β_{ITZ}	γ_{ITZ}	t_{ITZ}
0.5	0.5	0.8	0.1	0.001 mm

3. Material properties

3.1 Mortar

The physical properties of the mortar are presented in Supplementary Table **2**. To achieve a 100-MPa compressive strength, the Young's modulus, tensile strength, and fracture energy of the mortar were based on the values obtained using Eqs. (s12) and (s13): Eq. (s12) was obtained by fitting [23] the data obtained in previous research [59,47,61]. Eq. (s13) was obtained from the standards of the Japan Society for Civil Engineers[61].

$$E_{cm,macro} = 0.22 f_{cm,macro} + 13.4 \quad \text{(s12)}$$

$$G_{ftm,macro} = 0.01 \cdot f_{cm,macro}{}^{1/3} \cdot d_{max}{}^{1/3} \quad \text{(s13)}$$

where d_{max} is the maximum aggregate size in the concrete or mortar. The tensile strength of mortar $f_{tm,macro}$ was obtained to reproduce the compressive strength of the cylindrical specimen.

Supplementary Table 2. Macroscopic properties of the mortar

	$E_{cm,macro}$ (N/mm^2)	$f_{cm,macro}$ (N/mm^2)	$f_{tm,macro}$ (N/mm^2)	$G_{ftm,macro}$ (N/mm)
mortar	35,400	100	14.0	0.0794[1)]

For the calibration, three different meshes were made for a cylindrical specimen with a size of Ø75 × 150 mm^3, using the Voronoi tessellation with different seeds of a random algorithm for a loading experiment. The typical size of each mesh was 3.0 mm. The calculation results are summarized in Supplementary Table 3.

Supplementary Table 3. Comparison of macro and simulation results for compressive properties of mortar cylinder

	Target property	Calculation
$f_{cm\,(macro,sim)}$ (N/mm^2)	100.0	100.5 (0.27)
$E_{cm\,(macro,sim)}$ (kN/mm^2)	35.4	35.7 (0.02)

Note: values with ( ) represent standard deviation.

3.2 Aggregate

Two experiments were conducted. One investigated the impact of the Young's modulus of the coarse aggregate on the concrete compressive strength to understand how the stress distribution and resultant cracks occurred around the coarse aggregate. For calculation, the properties of the aggregates presented in **Supplementary Table 4** were used. In reality, the strength of the aggregate is also altered. In the subsequent analysis, the compressive strength of the aggregate was used as a parameter. The notation and corresponding physical properties of the aggregates are summarized in **Supplementary Table 5**. The tensile strength of the coarse aggregate ($f_{ta,macro}$) was calculated from the compressive strength ($f_{ca,macro}$) using the following equation[62]:

$$f_{ta,macro} = 0.06 f_{ca,macro} \quad \text{(s14)}$$

For calibration of the spring parameters, the stress–strain curves obtained from the axial compressive loading test on the aggregate samples from reference [63] were reproduced by adjusting the parameters c_a^* and β_0^*. The specimen size was Ø25 × 50 mm^3 and the typical element size was 2.4 mm, the same value used for the single-aggregate concrete specimen experiment and concrete compressive loading experiment. The obtained spring parameter rules shown in **Supplementary Table 3** can reproduce the target macroscopic aggregate properties (**Supplementary Table 5**) and sudden drop in post-peak behavior, a typical characteristic of rocks in concrete course aggregates[63]. The calculated results are summarized in Supplementary Figure 5

Supplementary Table 4. Coarse aggregate properties for numerical experiment on impact of Young's modulus of coarse aggregate on concrete compressive strength

	Notation of concrete	$E_{ca,macro}$ (N/mm^2)	$f_{ca,macro}$ (N/mm^2)	$f_{ta,macro}$ (N/mm^2)
Aggregate	E_{ca} = 0.01	10	1000.0*	1000.0*
	E_{ca} = 5	5000		
	E_{ca} = 15	15000		
	E_{ca} = 25	25000		
	E_{ca} = 35.4	35400		
	E_{ca} = 50	50000		
	E_{ca} = 70	70000		
	E_{ca} = 100	100000		
	E_{ca} = 250	250000		

Note: No fracture in aggregate was assumed in the target numerical experiment.

Supplementary Table 5. Coarse aggregate properties for numerical experiment on impact of coarse aggregate properties on concrete compressive strength

	Compressive strength (MPa)	Young's modulus (GPa)	Fracture energy (N/mm)	Calculated compressive strength (MPa)	Calculated Young's modulus (GPa)	Aggregate
CA1-40	40	100	0.022	40.1 (0.11)	101.1 (0.17)	Limestone
CA1-50	50			50.7 (0.09)	101.2 (0.30)	
CA1-75	75			77.1 (0.31)	101.0 (0.15)	
CA1-100	100			100.0 (0.36)	101.0 (0.15)	
CA1-150	150			152.1 (0.68)	100.9 (0.19)	
CA1-250	250			251.5 (1.24)	100.5 (0.15)	
CA2-40	40	70	0.030	40.0 (0.18)	71.0 (0.13)	Sandstone
CA2-50	50			50.7 (0.23)	71.0 (0.21)	
CA2-75	75			76.7 (0.29)	70.9 (0.10)	
CA2-100	100			99.4 (0.33)	70.9 (0.10)	
CA2-150	150			151.2 (0.64)	70.8 (0.10)	
CA2-250	250			250.1 (1.19)	70.5 (0.11)	
CA3-40	40	50	0.050	40.1 (0.20)	50.8 (0.07)	Granite
CA3-50	50			50.9 (0.04)	50.8 (0.13)	
CA3-75	75			77.7 (0.34)	50.7 (0.07)	
CA3-100	100			101.1 (0.37)	50.8 (0.07)	
CA3-150	150			153.1 (0.67)	50.7 (0.08)	
CA3-250	250			253.0 (1.08)	50.5 (0.09)	
CA4-40	40	35.4	0.063	40.0 (0.22)	36.1 (0.07)	Lightweight aggregate
CA4-50	50			50.7 (0.28)	36.0 (0.10)	
CA4-75	75			76.9 (0.36)	36.0 (0.05)	
CA4-100	100			99.6 (0.20)	36.0 (0.06)	
CA4-150	150			151.5 (0.67)	36.0 (0.06)	
CA4-250	250			250.4 (1.02)	35.8 (0.06)	
CA5-40	40	15	0.150	39.9 (0.30)	15.4 (0.06)	

CA5-50	50			50.3 (0.76)	15.4 (0.04)	Lightweight aggregate
CA5-75	75			76.8 (0.48)	15.5 (0.02)	
CA5-100	100			99.8 (0.45)	15.3 (0.02)	
CA5-150	150			151.3 (0.74)	15.3 (0.02)	
CA5-250	250			250.1 (1.10)	15.3 (0.03)	
CA6-40	40	5	0.250	38.9 (0.33)	5.1 (0.03)	Lightweight aggregate
CA6-50	50			49.1 (0.28)	5.2 (0.01)	

Note: values with ( ) represent standard deviation.

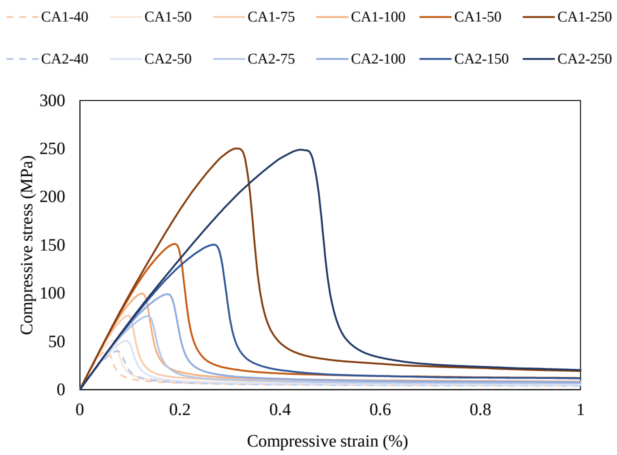

IN

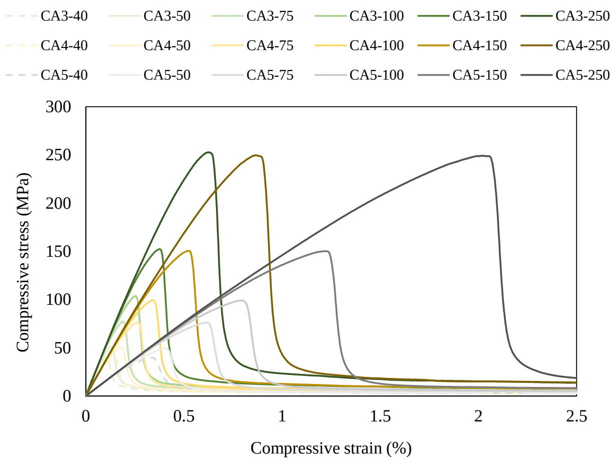

(a) (b)

Supplementary Figure 5. Stress–strain curve of (a) series of CA1 and CA2; (b) series of CA3, CA4, and CA5

The properties of coarse concrete aggregates have been investigated in previous studies. However, studies on the relationships between the compressive strength and Young's modulus of rock and mortar are limited. A summary based on references [29,30,31,32,33] is presented in **Supplementary Figure 6**. In the figure, there is significant scattering, especially for sandstone, a sedimentary rock that is used only when it is strong enough for concrete application. Limestone has lower compressive strength and the same Young's modulus range as quartz schist and sandstone. Andesite has a lower Young's modulus with a compressive stress range similar to that of sandstone. This characteristic makes andesite suitable for use in high-strength concrete because the Young's modulus of mortar is similar.

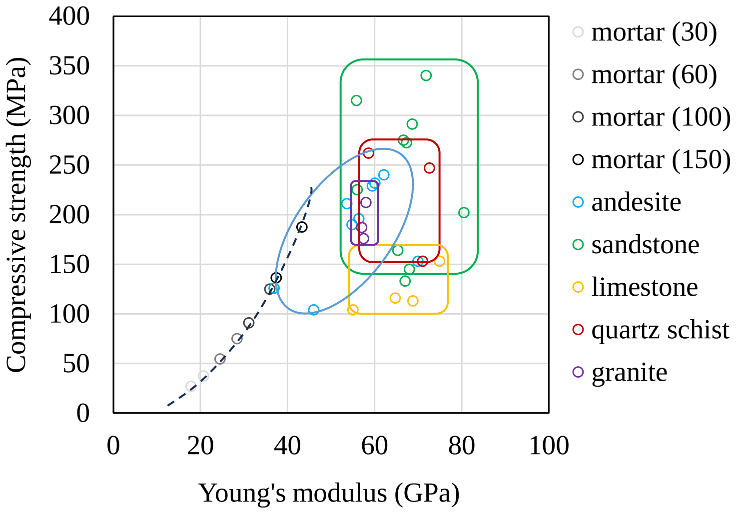

Supplementary Figure 6. **Relationships between compressive strength and Young's modulus of mortar and concrete coarse aggregate rock. The data were obtained from [29-33].**

4. Meshes

4.1 Single-aggregate specimen

The specimen size was Ø45 × 65 mm^3. A spherical aggregate with a diameter of 25 mm was placed at the center of the specimen. The specimens are shown in **Supplementary Figure 7**. The typical element sizes of the aggregate and mortar were 2.4 mm and 3.0 mm, respectively. Rigid plates were attached to both ends of the specimen, with a forced deformation of 25 $\mu\epsilon$/step. The connection between the elements on the ends and the rigid plates was made using springs with a stiffness that was the same as that of the mortar in the normal direction. The shear springs were reduced to 10^{-9} times to emulate the non friction condition. Three specimens were prepared to confirm reproducibility.

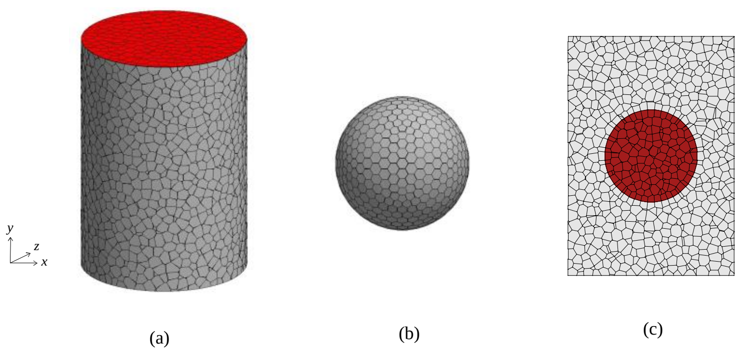

Supplementary Figure 7. Single-aggregate cylindrical specimen mesh: (a) axonometric view; (b) aggregate view; (c) section view of specimen

4.2 Concrete specimen

The compressive loading experiment was conducted using a specimen with a size of Ø75 × 150 mm^3. An overview of the specimens is presented in Supplementary Figure 8. The volumetric ratio of the coarse aggregate was 33.8% and the maximum aggregate size was 20 mm. The particle-size distribution of the aggregates satisfying Japanese industrial standard requirements (JISA5005:2020)[28] is shown in Supplementary Figure 9. To consider the effect of aggregate alignment on the compressive strength, three specimens were prepared, and the average value was used. The typical element sizes of the aggregate and mortar were 2.4 mm and 3.0 mm, respectively.

For compressive loading, rigid plates were attached on both ends of the specimen, with a forced deformation of 25 $\mu\epsilon$/step. The connection between the elements at the ends and the rigid plates was made using springs with a stiffness that was the same as that of the mortar in the normal and shear directions.

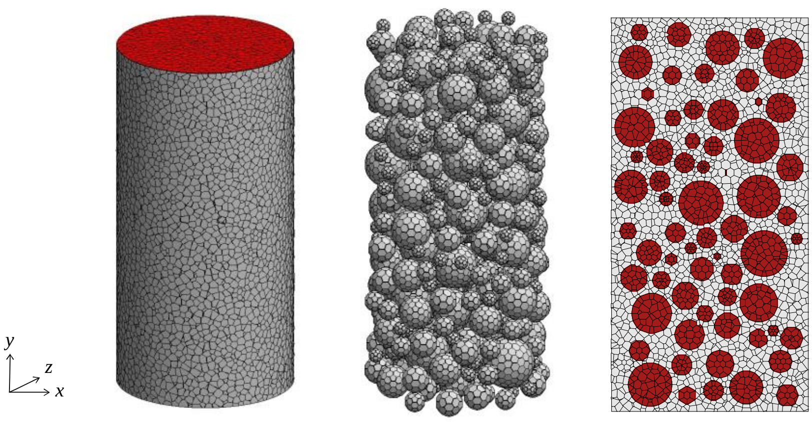

(a) (b) (c)

Supplementary Figure 8. Concrete specimen mesh: (a) axonometric view; (b) aggregate alignment; (c) section view of specimen

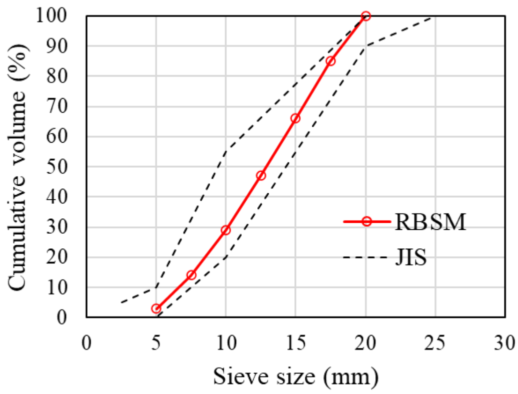

Supplementary Figure 9. Particle-size distribution of coarse aggregate in concrete specimen mesh

5. Impact of interfacial transition zone (ITZ) parameters

The effect of the ITZ on the physical properties of concrete is of great importance, and a research focus. Bleed water builds up beneath the aggregate particles; the resultant gap affects the compressive strength of the concrete[40]. In previous concrete studies, bleed water was generally created during specimen preparation; thus, the impact of bleed water was included. In one previous study, the compressive strength decreased as the maximum aggregate size increased[2,3]. A recent study showed an increase in the compressive strength with an increase in the maximum aggregate size[4,5,6]. This discrepancy can be attributed to the sample preparation. For high-strength concrete, the cement paste is generally viscous due to the superplasticizer, and the impact of the bleed-water gap on the compressive strength is dramatically reduced. Based on this experimental background, the impact of the ITZ on the results was studied. It is known that the ITZ thickness is increased when the aggregate size is large [39]. In our model, a uniform ITZ with different aggregate particle sizes was assumed. **Supplementary Figure 10**(a) shows the effect of t_{ITZ} on f_{cc}/f_{cm} with different E_{ca}/E_{cm} values, indicating that an increase in t_{ITZ} resulted in a slight decrease in f_{cc}/f_{cm}. However, there was no significant effect on the trend line.

Supplementary Figure 10(b) shows the impact of the physical properties of the ITZ. The reduction coefficients α_{ITZ} and η_{ITZ} were chosen at two different levels, with ITZ properties the same as and significantly inferior to those of the mortar. The trends were similar, although the maximum f_{cc}/f_{cm} values were different. If the ITZ was weak, the compressive strength was lower. These results are consistent with those from previous studies [19,20]. A peak near E_{ca}/E_{cm} = 1.0 was confirmed when the ITZ properties were inferior to those of the mortar, even though the decreasing trend of f_{cc}/f_{cm} was moderate.

Supplementary Figure 10(c) and (d) show the trend lines between E_{ca}/E_{cm} and f_{cc}/f_{cm} with two different levels of β_{ITZ} and different volume contents of coarse aggregate. β_{ITZ} = 0.8 indicates that the ITZ properties were similar to those of the mortar; the impact of aggregate volume on f_{cc}/f_{cm} was confirmed. β_{ITZ} = 0.4 indicates that the ITZ properties were inferior to those of the mortar; the impact of aggregate volume on f_{cc}/f_{cm} was confirmed. This suggests that in previous studies, normal-strength concrete was affected by the bleed-water gap.

Based on the calculation results, the selected ITZ parameters reasonably represented the characteristics of the prepared concrete specimens. In other words, even though the properties of the ITZ were altered, the overall trend observed in this study was not significantly affected.

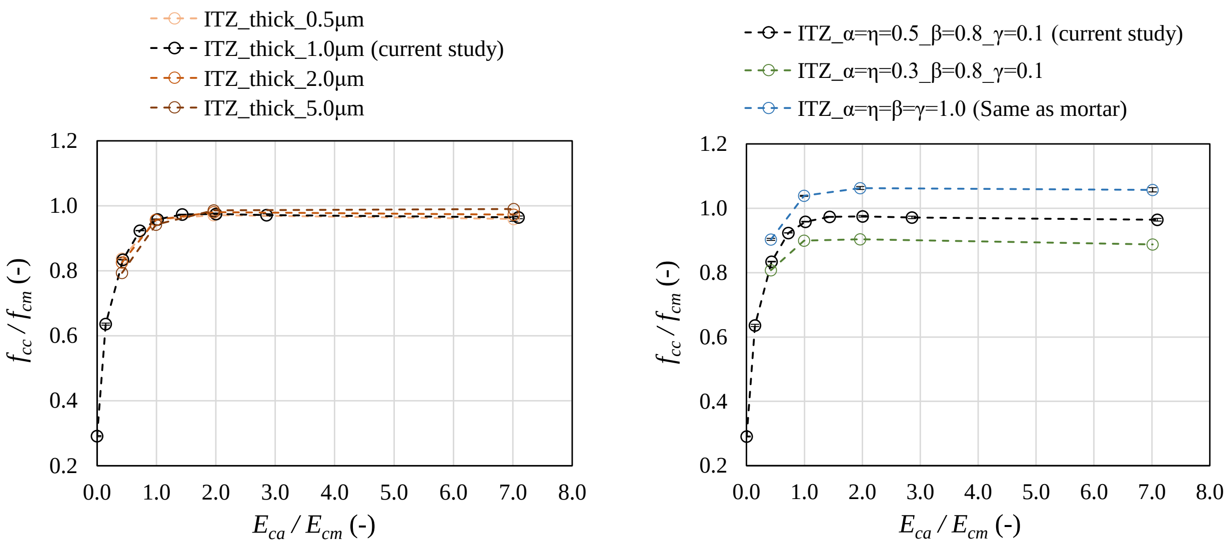

(a) (b)

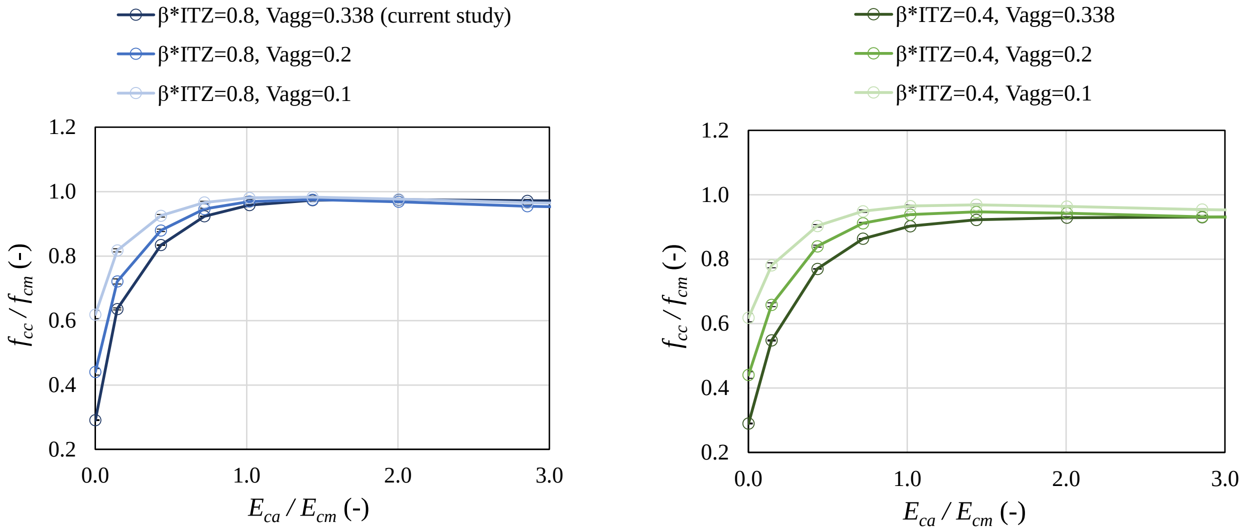

(c) (d)

Supplementary Figure 10. Studies on impact of ITZ parameters on obtained results: (a) Impact of nominal gap size (t_{ITZ}) around aggregate; (b) Impact of α_{ITZ} and η_{ITZ}; (c) Relationship between E_{ca}/E_{cm} and f_{cc}/f_{cm} with β_{ITZ} = 0.8 and different aggregate contents; (d) Relationship between E_{ca}/E_{cm} and f_{cc}/f_{cm} with β_{ITZ} = 0.4 and different aggregate contents

6. Evaluation of calculated data

The nondestructive aggregate case shows the envelope curves of the relationships between E_{ca}/E_{cm} and f_{cc}/f_{cm}. The envelope is represented by the following equation:

$$f_{cc}/f_{cm} = a_1 - a_2 \exp\left(-a_3\, E_{ca}/{E_{cm}}^{a_4}\right) \quad \text{(s15)}$$

where a_1 = 0.98, a_2 =0.68, a_3 =0.75, and a_4 =3.0. In the region where E_{ca}/E_{cm}<1.0, f_{cc}/f_{cm} increased exponentially as E_{ca}/E_{cm} increased. The fitting results are presented in **Supplementary Figure 11**(a).

The calculation results for cases allowing aggregate fracture can be categorized in two regions, as shown in **Supplementary Figure 11**(b). One is the region with f_{ca}/f_{cm} ≧1.0. In this region (region (I)), the slope of f_{ca}/f_{cm} against E_{ca}/E_{cm} in the region with E_{ca}/E_{cm} ≧1.0 increases from zero. The other region (region (II)) has f_{ca}/f_{cm}<1.0 and a constant slope. To reproduce this behavior, the calculated results at E_{ca}/E_{cm} ≒ 2.83 were corrected and the curve was fitted (**Supplementary Figure 11**(c)). The trend can be represented by the following equation:

$$f_{cc}/f_{cm} = b_1 - b_2 \exp\left(-b_3\, f_{ca}/{f_{cm}}^{b_4}\right) \quad \text{(s16)}$$

where b_1 = 0.98, b_2 =0.68, b_3 =1.6, and b_4 =1.5. Based on this curve, the slope in region (I) was obtained by connecting the intercept point on the Y-axis (0, 1.04) (determined from the fitting results) to the point at E_{ca}/E_{cm} = 2.83. In this case, the slope with f_{ca}/f_{cm} =1.0 was -0.0678. In region (II), based on a slope of -0.0678 and the point at E_{ca}/E_{cm} = 2.83 with a given f_{ca}/f_{cm}, the decreasing lines were determined. The curves for each f_{ca}/f_{cm} were calculated based on the envelope and decreasing line.

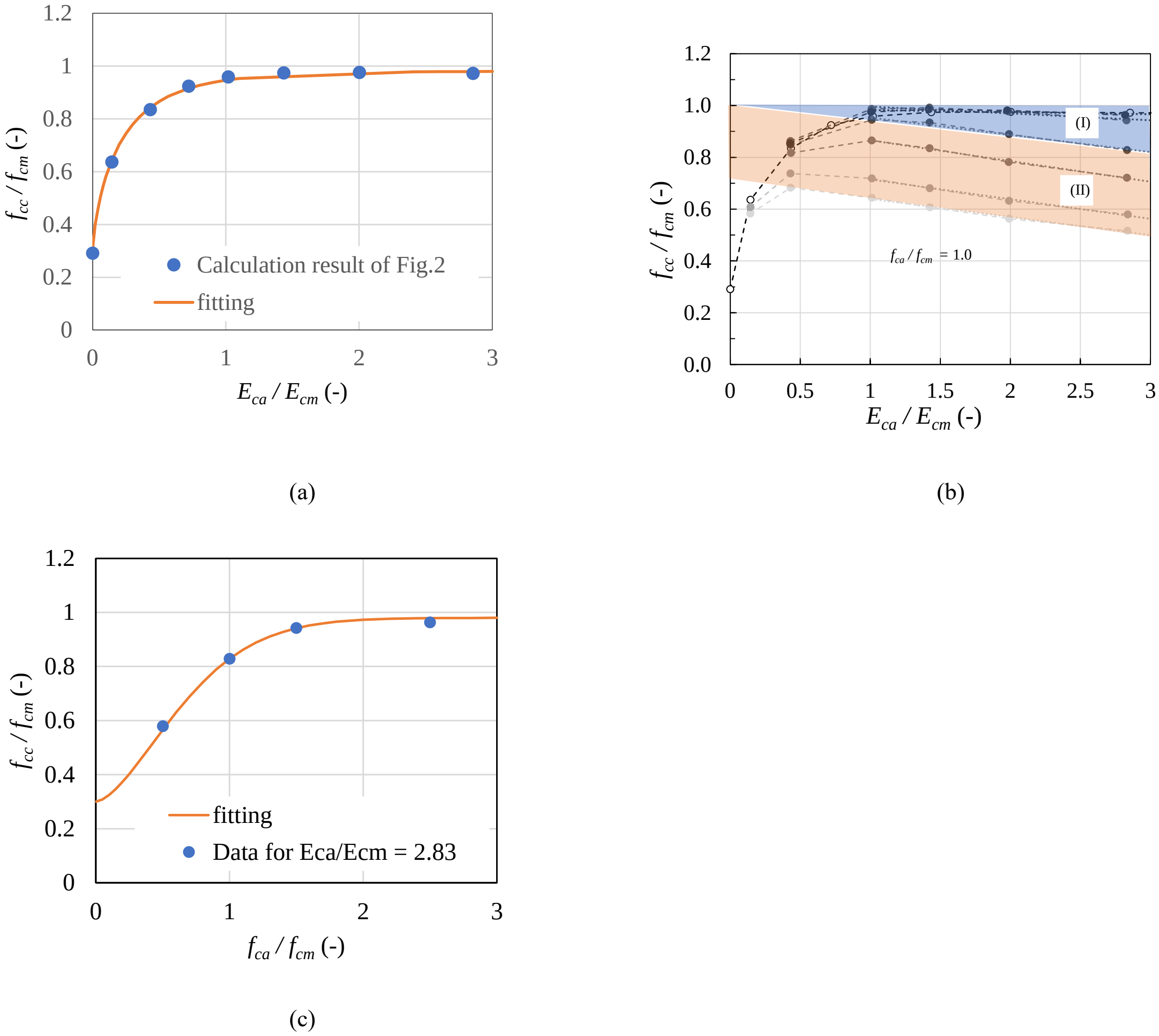

Supplementary Figure 11. Process of mapping relationships between E_{ca}/E_{cm} and f_{cc}/f_{cm}; (a) Envelope curve-fitting results for E_{ca}/E_{cm} and f_{cc}/f_{cm}; (b) Region definition; (c) Fitting for calculated data at $E_{ca}/E_{cm} \fallingdotseq 2.83$